(Received 13 January 2026, Accepted 4 February 2026, Scheduled 26 February 2026)

Compact Ultra-Wideband MIMO Antenna with High Isolation Based on Metamaterials with Mirror Symmetry

Xuemei Zheng[1], Shengbang Ma[2,*], and Linfei Yue[2]

[1]*Key Laboratory of Modern Power System Simulation and Control and Renewable Energy Technology, Ministry of Education, Northeast Electric Power University, Jilin, China*
[2]*School of Electrical Engineering, Northeast Electric Power University, Jilin, China*

ABSTRACT: This paper presents a low-coupling ultra-wideband (UWB) antenna based on a metamaterial structure. The proposed metamaterial exhibits single-negative characteristics with a negative permittivity (ε) in the 3.3–4 GHz and 6.4–10.1 GHz bands, effectively reducing inter-element coupling. Through simulation and experimental measurement, the antenna is demonstrated to operate from 3.1 to 11.4 GHz, achieving an absolute bandwidth of 11.31 GHz and a relative bandwidth of 114.5% ($S_{11} < -10$ dB). By integrating the metamaterial to suppress inter-element coupling, the antenna maintains low mutual coupling across the entire operating band ($S_{21} < -20$ dB), with an envelope correlation coefficient (ECC) below 0.0045 and a radiation efficiency ranging from 70% to 95%. These outstanding performance metrics render the antenna well-suited for indoor high-precision positioning scenarios, providing stable and high-speed data transmission capabilities.

1. INTRODUCTION

With the continuous evolution of wireless communication technologies, next-generation communication systems, including 5G and the Internet of Things (IoT) [1] have been extensively deployed worldwide. Wireless communication systems across diverse application scenarios have imposed increasingly stringent performance requirements on antenna designs, encompassing operating bandwidth, omnidirectional radiation characteristics, and inter-port signal isolation. Ultra-wideband (UWB) multiple-input multiple-output (MIMO) antennas [2] have emerged as a viable solution to meet these rigorous performance demands. However, the high integration density of antenna elements induces strong electromagnetic coupling among adjacent radiating units, which degrades the impedance matching, radiation gain and radiation pattern characteristics of the antenna array [3].

Accordingly, scholars have proposed various decoupling strategies. One category involves the introduction of grounding branches [4] or defected ground structures (DGS) [5] into the ground plane as decoupling configurations; another embed metamaterials [7] or electromagnetic bandgap (EBG) structures [6] either between or above the radiating elements to achieve mutual coupling suppression.

Ref. [8] proposed a dual-pentagonal radiating patch MIMO antenna, with a complementary split-ring resonator (CSRR) structure etched onto and integrated into the ground plane. This design achieves an isolation level in excess of -22 dB across the antenna's UWB operational bandwidth, albeit at the cost of degraded radiation directivity. Ref. [9] presented a broadband four-element metasurface-integrated MIMO antenna that attains an isolation of better than -23 dB. However, this antenna features an excessively large physical footprint of 178×178 mm^2, with radiating elements arranged in an orthogonal quadrilateral configuration, thus imposing significant constraints on its practical scalability. Ref. [10] proposed a quad-G-shaped metamaterial structure, which facilitates the antenna to achieve an isolation level exceeding -19 dB over the 4–12 GHz operational band, yet it offers no notable miniaturization merits. Ref. [11] introduced a UWB four-port metasurface-based MIMO antenna, while boasting a high-gain performance. This design succumbs to an overly large form factor and inadequate inter-element isolation, with the latter merely marginally exceeding -15 dB.

To address these issues, this study designs, simulates, and experimentally verifies a compact UWB high-isolation MIMO antenna. Decoupling is achieved through a metamaterial structure with mirror-symmetric semi-circular split-ring resonators — integrated on an FR-4 substrate and arranged as a 2×3 array above the antenna. Systematic optimization yielded an operating bandwidth of 3.1–11.4 GHz. Simulations and experiments show isolation > -20 dB across the band and improved radiation performance, demonstrating great potential for engineering applications.

2. ANTENNA AND METAMATERIAL DESIGN

2.1. MIMO Antenna Design

The radiating elements of the proposed MIMO antenna were printed on a 31 mm $\times$ 26 mm $\times$ 1.6 mm FR-4 dielectric substrate (with a relative permittivity $\varepsilon_r = 4.3$ and a dielectric loss tangent $\tan\delta = 0.02$). Its front side has two microstrip-

* Corresponding author: Shengbang Ma (2202400423@neepu.edu.cn).

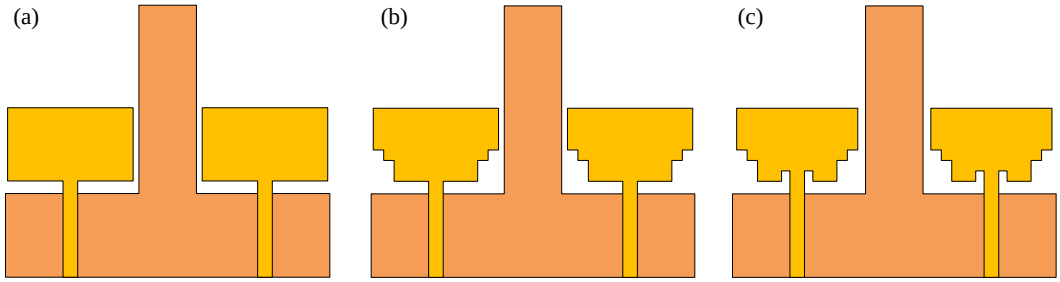

FIGURE 1. MIMO antenna design procedures: (a) Preliminary MIMO antenna; (b) Cut stepped Angle MIMO antenna; (c) Feed line etched rectangular notch MIMO antenna (The orange part represents the back structure.).

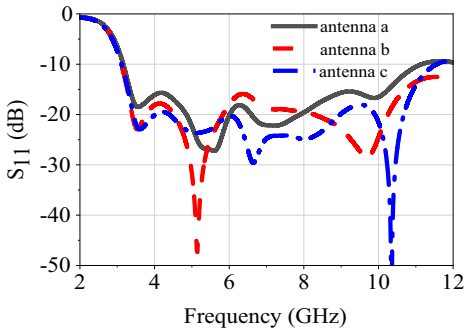

FIGURE 2. S-parameter analysis of antennas a, b, and c.

fed radiating patches, with stepped rectangular cutouts at their bottom-left and bottom-right corners and rectangular notches etched adjacent to the feed line; these features jointly extend the effective current path to enhance impedance matching in the mid-to-high frequency bands. The ground plane was an inverted-T-shaped defected ground structure (DGS), and the antenna's design workflow is illustrated in Fig. 1. As depicted in Fig. 2, the antenna achieves a return loss below -15 dB over 3.2–10.8 GHz, with an impedance-matched bandwidth of 3.1–11.4 GHz (relative bandwidth: 114.5%). Its optimized structural dimensions, determined through parametric analysis and performance trade-off optimization, are presented in Fig. 3. The specific values are presented in Table 1.

TABLE 1. Dimensions of the optimized antenna structure. (unit: mm).

Parameters	Size	Parameters	Size	Parameters	Size
L	26	L_5	8	W_2	1
L_1	7	L_6	9.2	W_3	0.8
L_2	3	L_7	18	W_4	1.4
L_3	2	W	31	W_5	5.5
L_4	1	W_1	12		

2.2. Design and Analysis of Metamaterial Units

Metamaterials are artificially engineered composite structural materials, whose electromagnetic properties are governed predominantly by their structural configurations and dimensional parameters. The entire metamaterial structure can be equivalently modeled as an LC resonant circuit. Inductance (L) is mainly determined by the total current path length of the metallic ring; a larger circumference results in higher inductance. Capacitance (C), in turn, mainly comes from the ring's two central slots and its opening gap width; narrower slots mean larger capacitance. This LC resonance induces effective negative permittivity ($\varepsilon < 0$), where electromagnetic waves at the resonant frequency cannot propagate effectively through the structure, forming a transmission stopband. Specifically, within the operating band, metamaterials use their surface wave bandgap properties to prevent substrate-integrated antenna surface waves from leaking into free space and converting into space waves, thus eliminating the resulting secondary coupling [12]. This study proposes a single-layer metamaterial unit cell exhibiting electromagnetic resonance near 3.3 GHz (as illustrated in Fig. 4). Employing a mirror-symmetric hook-shaped semicircular resonator topology, a single circular split ring is divided into two symmetric semi-circular split rings, which are coupled and interconnected via horizontal metallic strips.

As shown in Fig. 5, the metamaterial structure was optimized in CST Microwave Studio. It was modeled on a 1.6-mm-thick FR-4 substrate enclosed in an air box. In the simulation, waveguide ports were assigned to the boundaries perpendicular to the Z-axis for excitation. The surfaces normal to the Y-axis were set as perfect magnetic conductors (Perfect H), and those perpendicular to the X-axis were defined as perfect electric conductors (Perfect E) [13]. The optimized geometric parameters were as follows: the substrate dimensions were $W_s = L_s = 8.5$ mm; the metallic strip width was $V_s = 0.2$ mm. For the split-ring resonator, the outer radius $r_2 = 4$ mm, the inner radius $r_1 = 3.5$ mm, and the gap width $D = 1.1$ mm. The hook-shaped strip had a width $V = 0.6$ mm and a length $L_f = 3.2$ mm, as determined through simulation-based optimization.

2.3. Simulation Analysis

The metamaterial element's S-parameters were obtained from the CST simulations (Fig. 6(a)). To further investigate its electromagnetic properties, the S-parameter inversion method [7, 14] was used to extract the equivalent parameters of the equivalent homogeneous medium, with results shown in Fig. 6(b). The S-parameter extraction procedure is as follows.

The reflection coefficient is denoted as S_{11}, and the correlation between S_{21} and transmission coefficient T can be ex-

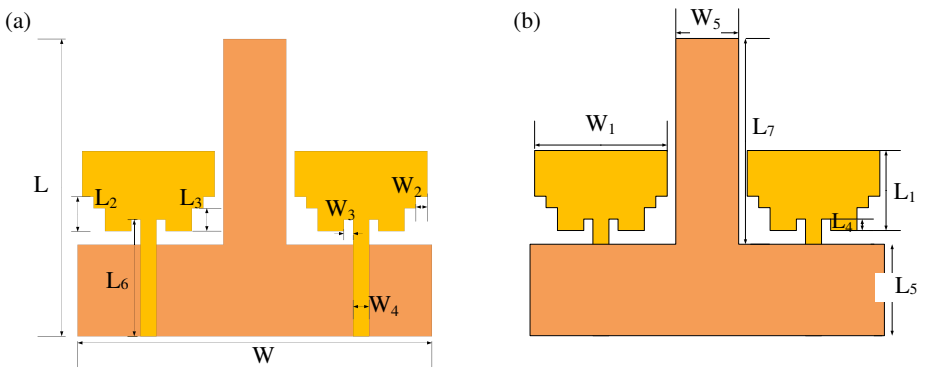

FIGURE 3. MIMO antenna structure diagram. (a) Front structure of the antenna. (b) Back structure of the antenna.

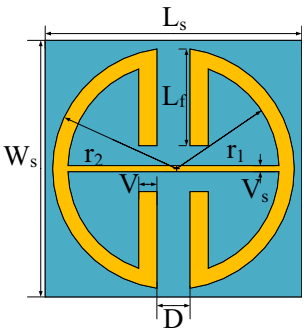

FIGURE 4. Structural diagram of metamaterial.

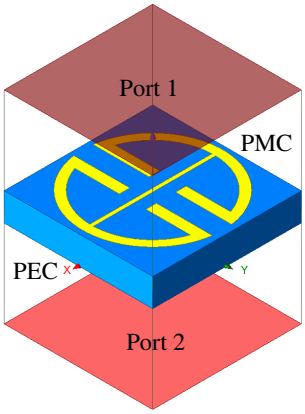

FIGURE 5. Waveguide simulation metamaterials.

pressed as:

$$S_{21} = Te^{ik_0 d} \tag{1}$$

where k_0 denotes the incident wave number in free space; d represents the thickness of the uniform dielectric plate; and the S-parameters are associated with the refractive index n and impedance z as given below:

$$S_{11} = \frac{R_{01}(1-e^{i2nk_0 d})}{1-R_{01}^2 e^{i2nk_0 d}} \tag{2}$$

$$S_{21} = \frac{(1-R_{01}^2)e^{ink_0 d}}{1-R_{01}^2 e^{i2nk_0 d}} \tag{3}$$

where $R_{01} = \frac{Z-1}{Z+1}$, the inversion of Eq. (2) and Eq. (3) leads to:

$$Z = \pm\sqrt{\frac{(1+S_{11})^2 - S_{21}^2}{(1-S_{11})^2 - S_{21}^2}} \tag{4}$$

$$e^{ink_0 d} = X \pm i\sqrt{1-X^2} \tag{5}$$

where $X = \frac{1}{2[S_{21}(1-S_{11}^2+S_{21}^2)]}$. Since the considered metamaterial is a passive medium, z and n in Eq. (4) and Eq. (5) satisfy:

$$\mathrm{Re} \geq 0 \tag{6}$$

$$\mathrm{Im}(n) \geq 0 \tag{7}$$

Therefore, the value of the refractive index n can be obtained from Eq. (5):

$$n = \frac{1}{k_0 d}\left\{\left[\mathrm{Im}\left[\ln(e^{ink_0 d})\right] + 2m\pi\right] - i\mathrm{Re}\left[\ln(e^{ink_0 d})\right]\right\} \tag{8}$$

where m denotes an integer associated with $\mathrm{Re}(n)$, and the two parameters that determine the properties of the metamaterial are obtained from Eqs. (9) and (10).

Magnetic permeability:

$$\mu = nz \tag{9}$$

Dielectric constant:

$$\varepsilon = n/z \tag{10}$$

Figure 6(b) presents the frequency-dependent variations of the equivalent permittivity and permeability extracted via the waveguide simulation. As observed from the figure, the proposed metamaterial demonstrates negative equivalent permittivity in both the 3.3–4 GHz and 6.4–10.1 GHz bands, qualifying it as an epsilon-negative metamaterial.

2.4. Metamaterial Array Structure

Despite optimizations of the patch cutouts and defected ground structures, the inter-port isolation of the antenna within the 3.1–3.8 GHz band remained insufficient to meet the $\leqslant -20$ dB specification. Consequently, a decoupling metamaterial array was introduced between the radiating elements. As illustrated in Fig. 7, to ensure effective homogenization of the metamaterial, the unit-cell spacing was constrained to be below $\lambda/10$ at the operating frequency, while the overall array length was kept within the footprint of the MIMO antenna. Through simulation-based optimization using CST software, the parameters were

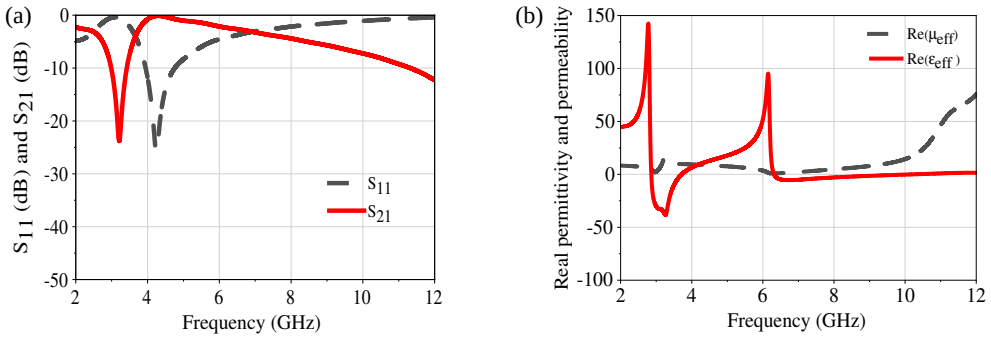

FIGURE 6. Parameter analysis of metamaterials. (a) S-parameters of metamaterials. (b) Dielectric constant and magnetic permeability of metamaterials.

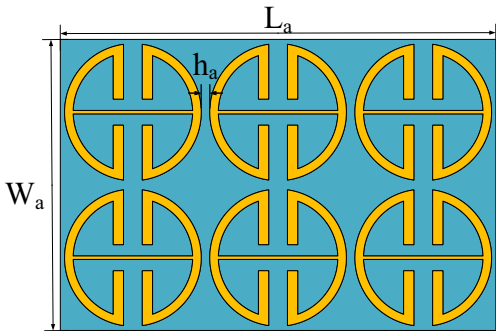

FIGURE 7. Structural diagram of the metamaterial array.

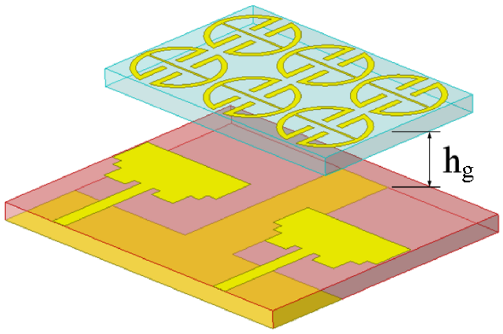

FIGURE 8. Structural diagram of the MIMO antenna.

determined as $L_a = 25.5$ mm, $W_a = 17$ mm, and the spacing $h_a = 0.5$ mm.

3. OVERALL STRUCTURE AND RESULT ANALYSIS OF THE MIMO ANTENNA

The overall configuration of the MIMO antenna is shown in Fig. 8, where $h_g = 8$ mm (h_g denotes the height of the ground plane). To maintain comparability between the measured results, the metamaterial-alloaded antenna and the original antenna share identical structural dimensions.

3.1. Parameter Analysis of Antenna Dimensions

To guarantee the antenna's optimal operational performance, it is essential to analyze its dimensional parameters, thereby achieving a balance between impedance matching and isolation.

To investigate the impact of radiation element size on impedance matching and isolation, this study performs parametric analysis on the radiation element width L_1 while keeping the radiation element spacing unchanged. Fig. 9 presents the parametric analyses of the antenna's S_{11} and S_{21} parameters under different L_1 values. As observed in Fig. 9, Impedance matching and isolation at 7 mm have improved relative to those at 6.5 mm; however, with respect to impedance matching in the 3–5 GHz and 8–10 GHz bands, the 7 mm design offers no advantage over the 7.5 mm and 8 mm configurations. In contrast, it achieves superior isolation in the 3–5 GHz and 7–10 GHz bands, while maintaining comparable isolation performance across all other frequency bands. Considering the performance balance between the two, 7 mm is selected as the optimal value for L_1.

3.2. S-Parameter Simulation Analysis

The simulation results of the UWB MIMO antenna after parameter optimization are shown in Fig. 10. As observed from the figure, after integrating the metamaterial structure, the antenna bandwidth ranges from 3.1 to 11.4 GHz without any degradation or narrowing. Furthermore, the reflection coefficients (S_{11}) over the frequency range of 3.2 to 10.8 GHz all remain below -15 dB, preserving the excellent impedance matching performance of the original antenna. As illustrated in Fig. 10(b), after integrating the metamaterial decoupling structure, the antenna isolation is significantly enhanced over the range of 2.5 to 4 GHz, with a modest improvement in the 7 to 9.5 GHz band; the isolation within this range all remains below -25 dB. The maximum enhancement was achieved at 3.3 GHz, increasing from 18.5 dB to 28 dB (an improvement of 9.5 dB). Even outside the operating bandwidth of the metamaterial, it enables antenna isolation to be maintained below -20 dB. The full-band isolation is improved from above 18.5 dB to over 20 dB, which fully validates the effectiveness of the proposed metamaterial decoupling structure.

3.3. Antenna Surface Current Analysis

To gain a more intuitive understanding of the decoupling mechanism in the metamaterial-loaded antenna, a detailed analysis of the surface current distribution was conducted (as illustrated in

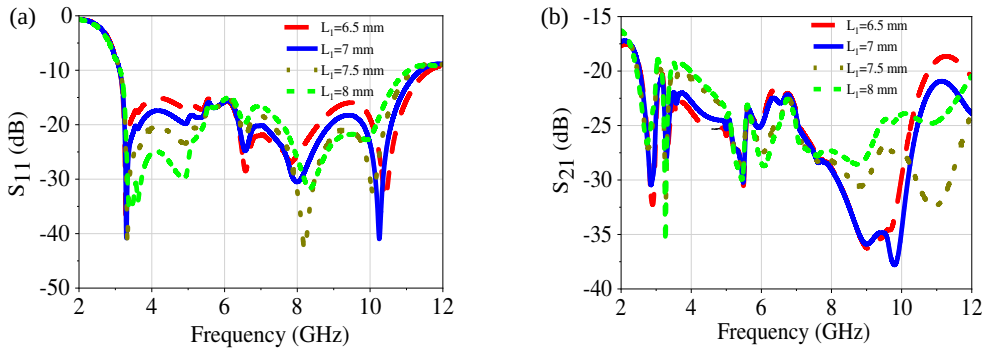

FIGURE 9. S-parameter scanning results. (a) S_{11} values under different L_1 values. (b) The S_{21} value under different L_1 values.

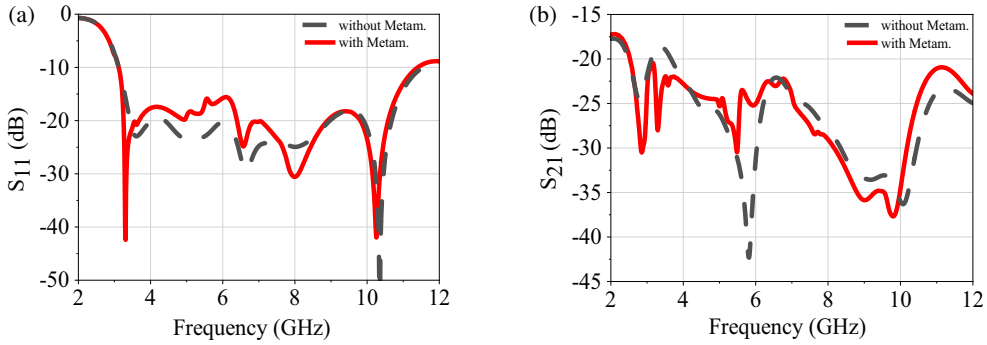

FIGURE 10. S-parameters of the metamaterial-loaded MIMO antenna. (a) S_{11} parameter. (b) S_{21} parameter.

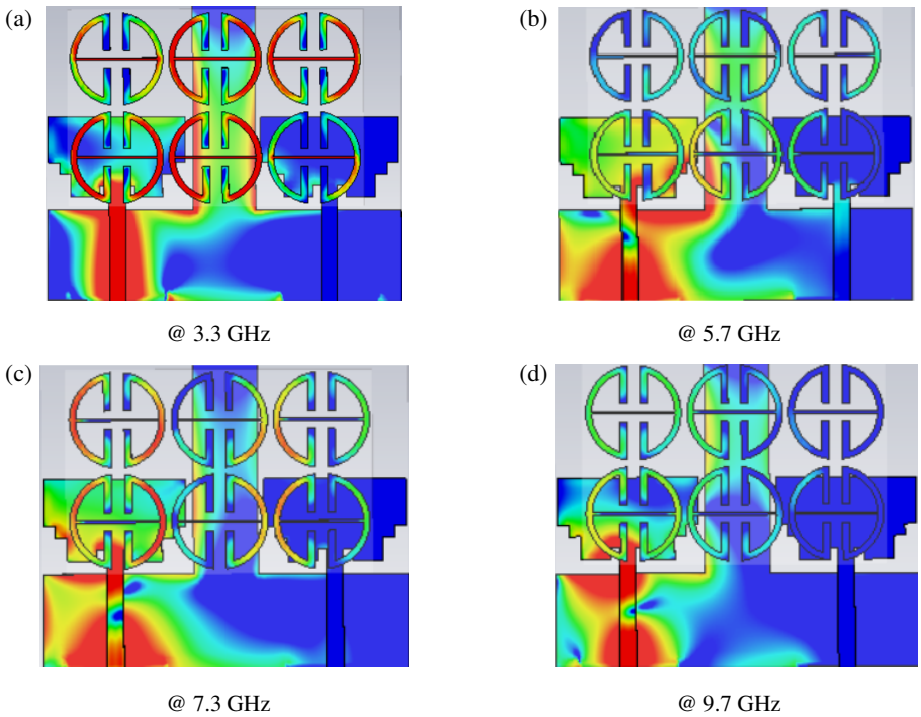

FIGURE 11. Surface current diagram of the antenna.

Fig. 11). It can be observed that when the antenna operates at 3.3 GHz and 7.3 GHz, the surface currents are predominantly concentrated on the semicircular ring and the intermediate connecting structure of the metamaterial. At 9.7 GHz, a significant current concentration is still maintained, indicating that the bandgap effect of the metamaterial design blocks the surface waves. Consequently, the coupled currents cannot propagate between the radiating elements and are instead absorbed by

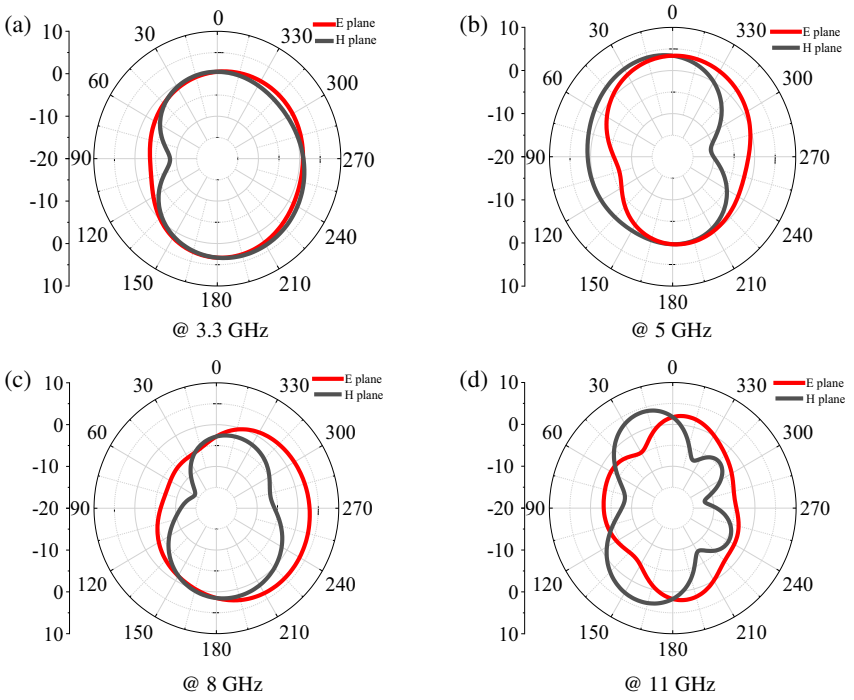

FIGURE 12. The radiation pattern of the antenna.

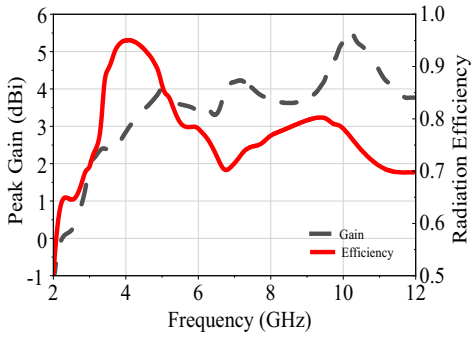

FIGURE 13. Gain and efficiency of proposed antenna.

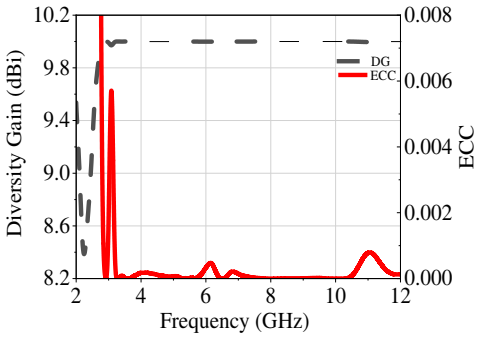

FIGURE 14. The ECC and the diversity gain value.

the resonant structures of the metamaterial, forming regions of concentrated current. However, at 5.7 GHz, although the metamaterial absorbs a portion of the electromagnetic energy, it is insufficient to prevent radiative coupling between the elements. Nevertheless, across most of the operating frequency bands, the metamaterial-based decoupling structure successfully suppresses mutual coupling by absorbing the electromagnetic energy transferred between adjacent radiating units.

3.4. Antenna Radiation Pattern

For a more intuitive analysis of the antenna's far-field radiation characteristics, the E-plane and H-plane radiation patterns were evaluated at 3.3 GHz, 5 GHz, 8 GHz, and 11 GHz, with the simulated results presented in Fig. 12. The results show that the antenna exhibits omnidirectional radiation at all four frequencies: At 3.3 GHz, there is a depression at 90°; at 5 GHz, there is a depression at 270°; and at 8 GHz, there is a depression at 60°. However, these minor depressions do not significantly degrade the overall omnidirectionality. At 11 GHz, the radiation pattern starts to distort, mainly owing to higher-order mode excitation in the high-frequency band, which causes uneven surface current density distribution. Nonetheless, the radiation performance still meets engineering requirements.

3.5. Antenna Gain and Radiation Efficiency

The gain and radiation efficiency characteristics of the antenna across the entire operating frequency band are shown in Fig. 13. As shown in the figure, it can be seen that the antenna delivers a gain of 2–5.6 dB across the 3.1–11.4 GHz band, with the peak gain recorded at 7 GHz and the minimum at 3.1 GHz. Over the full operational bandwidth, the radiation efficiency remains within the 70%–95% range, which means that most of the input energy from the feed is radiated effectively by the antenna. The antenna demonstrated a fairly high gain and radiation efficiency throughout the working frequency band, confirming its excellent radiation performance.

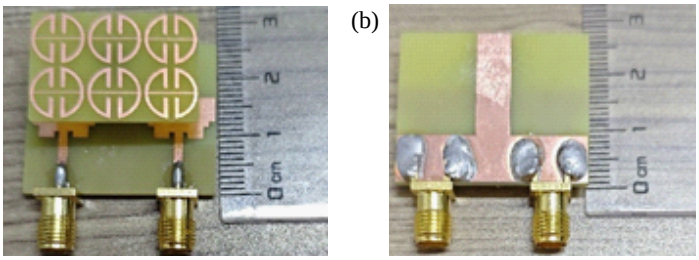

FIGURE 15. Physical processing diagram of the antenna. (a) Front view. (b) back view.

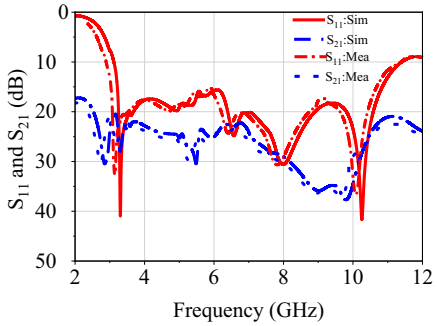

FIGURE 16. Measured and simulated values of the S-parameters.

TABLE 2. Comparison of parameters between the proposed design and similar designs.

References	Size/mm^2	Port	Bandwidth/GHz	Isolation/dB	ECC	Decoupling Technology
[5]	40×40	4	$2.57 \sim 12.2$	> 14	< 0.125	DGS
[10]	26×16.3	2	$4 \sim 12$	≥ 17	< 0.2	SRR
[11]	80×80	4	$3.2 \sim 7.6$	≥ 15.5	< 0.004	Metasurface
[15]	46×46	2	$3.1 \sim 11.7$	≥ 16.5	< 0.057	Neutral Line
[16]	52×26	2	$2.3 \sim 11.5$	≥ 16	< 0.012	Parasitic Branch
[17]	58×58	4	$2.8 \sim 12.1$	> 15	< 0.005	Grounding Branch
[18]	48×35	2	$2 \sim 18$	> 20	< 0.07	SRR
[19]	45×45	4	$3.1 \sim 11$	> 16	< 0.04	Rectangular patch
[20]	36×18	2	$2 \sim 11$	> 20	< 0.05	Slotted Branch
[21]	30×18	2	$4.3 \sim 15.6$	> 20	< 0.0075	Grounding Branch
[22]	30×35	2	$2 \sim 13.7$	> 20	< 0.15	Slotted Branch
This Work	31×26	2	$3.1 \sim 11.5$	> 20	< 0.0045	Metamaterial

3.6. MIMO Antenna Diversity Characteristics

For MIMO antenna arrays, it is essential to evaluate their envelope correlation coefficient (ECC) to assess the isolation and channel correlation: a lower ECC value indicates a reduced mutual coupling between antenna elements. The ECC ranged from 0 to 1, with a threshold of 1 for acceptable performance. The ECC can be calculated using Eq. (11):

$$\rho_e = \frac{\left|S_{11}^* S_{12} + S_{21}^* S_{22}\right|^2}{\left(1-\left(\left|S_{11}\right|^2+\left|S_{21}\right|^2\right)\right)\left(1-\left(\left|S_{11}\right|^2+\left|S_{21}\right|^2\right)\right)} \quad (11)$$

where S_{11}^* and S_{21}^* represent the real parts of parameters S_{11} and S_{21}, respectively. S_{12}^* and S_{21}^* represent the real parts of parameters S_{12} and S_{22}, respectively.

The diversity gain (DG) is another key parameter used to characterize MIMO antennas, reflecting their spatial diversity performance. A higher diversity gain signifies a more effective improvement in the system reliability and signal quality provided by MIMO technology, and it can be computed according to Eq. (12):

$$DG = \sqrt{1 - (\mathrm{ECC})^2} \quad (12)$$

Figure 14 shows the simulated ECC and diversity gain curves of the MIMO antenna. As illustrated in Fig. 15, the ECC remained below 0.0045 across the entire operating frequency band, and all values dropped below 0.001 above 3.2 GHz. This indicates that the designed MIMO antenna achieved excellent port isolation and performed optimally in multipath fading environments. Furthermore, the diversity gain within the operational band reaches up to 9.97 dBi, confirming outstanding diversity characteristics.

3.7. MIMO Antenna Physical Testing Analysis

A prototype antenna is fabricated and experimentally characterized to validate the efficacy of the proposed design. The prototype, constructed based on the optimized parameters described earlier, is shown in Fig. 15. The S-parameters of the antenna were characterized with an Agilent vector network analyzer (VNA), and simulated and measured results are comparatively presented in Fig. 16. A minor frequency offset is observed between the simulated and measured responses, arising from SMA connector losses, fabrication tolerances and environmental disturbances during the measurement process. Such discrepancies are nonetheless negligible, with the measured results exhibiting good consistency with the simulated ones. This validates the stable performance of the proposed MIMO antenna, with all deviations falling within acceptable engineering tolerances. Specifically, the antenna realizes an operating band-

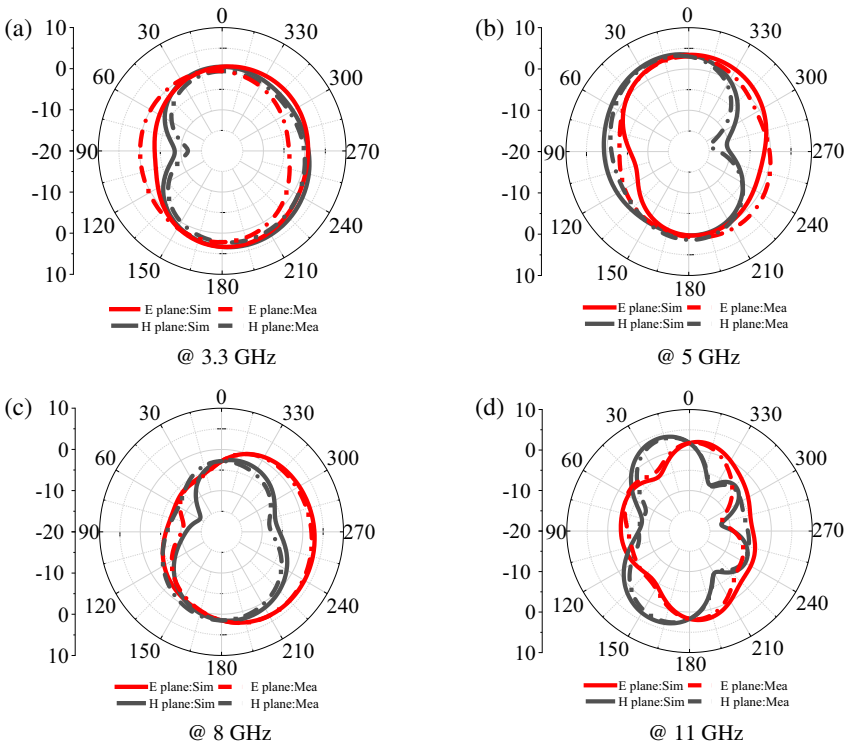

FIGURE 17. Measured and simulated radiation patterns.

width of 3.1–11.4 GHz with $S_{11} < -10$ dB and $S_{21} < -20$ dB, which fully meets the design specifications.

Figure 17 presents the simulated and measured radiation patterns of the antenna at 3.3 GHz, 5 GHz, 8 GHz, and 11 GHz. The obtained results confirm that the far-field radiation characteristics of the antenna meet the design requirements for the targeted frequency bands.

4. DISCUSSION

Table 2 presents a performance comparison between the MIMO antenna proposed in this work and designs reported in other publications. Key metrics for comparison include antenna dimensions, operating bandwidth, number of ports, isolation, and envelope correlation coefficient (ECC). Compared to the designs in [5, 11, 15–19], the proposed antenna achieves more compact dimensions and superior isolation. Furthermore, it exhibits a lower ECC than those in [10, 20–22], indicating weaker inter-element coupling and stronger unit independence. The tabulated data demonstrates that the antenna design presented herein offers advantages over all the referenced designs.

5. CONCLUSION

This paper proposes a UWB MIMO antenna featuring a metamaterial-based decoupling mechanism. The antenna operates across the 3.1–11.4 GHz frequency band and demonstrates excellent impedance matching, with an S_{11} below -15 dB, particularly within the 3.2–10.8 GHz range. A mirror-symmetric hook-shaped semi-circular split-ring metamaterial decoupling structure is introduced, which enables the antenna to achieve port isolation better than -20 dB over the entire operational band. Furthermore, the isolation is maintained below -25 dB within the 7–9.5 GHz sub-band, confirming the effectiveness of the decoupling design.

The proposed antenna is highly suitable for indoor high-precision positioning applications. It has very low ECC and high isolation ($S_{21} < -20$ dB) across the full band effectively, which suppress multipath interference and inter-element coupling, thereby ensuring the phase consistency of positioning signals. The compact form factor allows for integration into miniaturized positioning terminals. A radiation efficiency of 70–95% ensures sufficient signal transmission range and positioning accuracy. Additionally, the antenna's low mutual coupling and favorable gain characteristics guarantee stable and high-speed data transmission in complex electromagnetic environments.

ACKNOWLEDGEMENT

This study was funded by the National Natural Science Foundation of China (Grant No. 61803356). This study was supported by the Jilin Provincial Department of Education Science Research Project, (Project Number: JJKH20261429KJ).

REFERENCES

[1] Shafique, K., B. A. Khawaja, F. Sabir, S. Qazi, and M. Mustaqim, "Internet of things (IoT) for next-generation smart systems: A review of current challenges, future trends and prospects for emerging 5G-IoT scenarios," *IEEE Access*, Vol. 8, 23 022–23 040, 2020.

[2] El Tayeb, M. M., D. A. E. H. Salem, A. R. Mahmoud, I. M. Ibrahim, A. J. A. Al-Gburi, and M. H. M. Mahmoud, "A compact 4-ports UWB MIMO antenna with WiMAX and WLAN band re-

jection characteristics," *Progress In Electromagnetics Research C*, Vol. 160, 9–19, 2025.

[3] Chen, X., S. Zhang, and Q. Li, "A review of mutual coupling in MIMO systems," *IEEE Access*, Vol. 6, 24 706–24 719, 2018.

[4] Thotakura, H., R. Gogineni, K. S. Rao, C. K. Kumar, R. B. Sadineni, and S. Mandava, "A miniaturized highly isolated two port triple band-notched UWB MIMO antenna verified by characteristic mode analysis," *Progress In Electromagnetics Research C*, Vol. 160, 133–142, 2025.

[5] Thanki, P., T. Upadhyaya, U. Patel, V. Sorathiya, and M. Khishe, "Planar compact four port MIMO antenna for Ultra Wideband applications," *PLoS ONE*, Vol. 19, No. 12, e0314193, 2024.

[6] Kumar, N., U. K. Kommuri, and P. Usha, "Mutual coupling reduction in multiband MIMO antenna using cross-slot fractal multiband EBG in the E-plane," *Progress In Electromagnetics Research C*, Vol. 132, 1–10, 2023.

[7] Zheng, X., Z. Zhao, Y. Zhang, T. Zhang, A. Gui, and H. Wu, "A low-coupling broadband MIMO array antenna design for Ku-band based on metamaterials," *Journal of Electromagnetic Engineering and Science*, Vol. 24, No. 6, 666–673, 2024.

[8] Tighilt, Y., C. Bensid, D. Sayad, S. Mekki, R. Zegadi, M. L. Bouknia, I. Elfergani, P. Singh, J. Rodriguez, and C. Zebiri, "Low-profile UWB-MIMO antenna system with enhanced isolation using parasitic elements and metamaterial integration," *Electronics*, Vol. 12, No. 23, 4852, 2023.

[9] Salehi, M. and H. Oraizi, "Wideband high gain metasurface-based 4T4R MIMO antenna with highly isolated ports for sub-6 GHz 5G applications," *Scientific Reports*, Vol. 14, No. 1, 14448, 2024.

[10] Urimubenshi, F., D. B. O. Konditi, J. de Dieu Iyakaremye, P. M. Mpele, and A. Munyaneza, "A novel approach for low mutual coupling and ultra-compact Two Port MIMO antenna development for UWB wireless application," *Heliyon*, Vol. 8, No. 3, e09057, 2022.

[11] Hasan, M. M., M. T. Islam, M. Samsuzzaman, M. H. Baharuddin, M. S. Soliman, A. Alzamil, I. I. M. A. Sulayman, and M. S. Islam, "Gain and isolation enhancement of a wideband MIMO antenna using metasurface for 5G sub-6 GHz communication systems," *Scientific Reports*, Vol. 12, No. 1, 9433, 2022.

[12] Zheng, X., L. Yue, and Y. Zhang, "A compact four-port axially symmetric UWB-MIMO antenna array: Metamaterial-integrated coplanar waveguide for broadband operation with high isolation," *Progress In Electromagnetics Research C*, Vol. 162, 58–69, 2025.

[13] Zheng, X., Z. Zhao, Y. Pan, and T. Zhang, "Design of a miniaturized symmetrical E-shaped MIMO antenna with low coupling," *Applied Computational Electromagnetics Society Journal (ACES)*, Vol. 39, No. 12, 2024.

[14] Numan, A. B. and M. S. Sharawi, "Extraction of material parameters for metamaterials using a full-wave simulator [education column]," *IEEE Antennas and Propagation Magazine*, Vol. 55, No. 5, 202–211, 2013.

[15] Dkiouak, A., M. E. Ouahabi, S. Chakkor, M. Baghouri, A. Zakriti, and Y. Lagmich, "High performance UWB MIMO antenna by using neutralization line technique," *Progress In Electromagnetics Research C*, Vol. 131, 185–195, 2023.

[16] Kiani, S. H., H. S. Savci, M. E. Munir, A. Sedik, and H. Mostafa, "An ultra-wide band MIMO antenna system with enhanced isolation for microwave imaging applications," *Micromachines*, Vol. 14, No. 9, 1732, 2023.

[17] Khan, O., S. Khan, S. N. K. Marwat, N. Gohar, M. Bilal, and M. Dalarsson, "A novel densely packed 4 × 4 MIMO antenna design for UWB wireless applications," *Sensors*, Vol. 23, No. 21, 8888, 2023.

[18] Sakli, H., C. Abdelhamid, C. Essid, and N. Sakli, "Metamaterial-based antenna performance enhancement for MIMO system applications," *IEEE Access*, Vol. 9, 38 546–38 556, 2021.

[19] Kumar, S., G. H. Lee, D. H. Kim, W. Mohyuddin, H. C. Choi, and K. W. Kim, "A compact four-port UWB MIMO antenna with connected ground and wide axial ratio bandwidth," *International Journal of Microwave and Wireless Technologies*, Vol. 12, No. 1, 75–85, 2020.

[20] Khan, M. I. and M. I. Khattak, "Designing and analyzing a modern MIMO-UWB antenna with a novel stub for stop band characteristics and reduced mutual coupling," *Microwave and Optical Technology Letters*, Vol. 62, No. 10, 3209–3214, 2020.

[21] Mu, W., H. Lin, Z. Wang, C. Li, M. Yang, W. Nie, and J. Wu, "A flower-shaped miniaturized UWB-MIMO antenna with high isolation," *Electronics*, Vol. 11, No. 14, 2190, 2022.

[22] Altaf, A., A. Iqbal, A. Smida, J. Smida, A. A. Althuwayb, S. H. Kiani, M. Alibakhshikenari, F. Falcone, and E. Limiti, "Isolation improvement in UWB-MIMO antenna system using slotted stub," *Electronics*, Vol. 9, No. 10, 1582, 2020.